Journal of
Materials Chemistry A

ROYAL SOCIETY
OF CHEMISTRY

PAPER

Cite this: *J. Mater. Chem. A*, 2022, **10**, 234

Influence of intrinsic defects on the structure and dynamics of the mixed Pb–Sn perovskite: first-principles DFT and NAMD simulations†

Qi Liu,[ab] Akang Li,[ab] Weibin Chu,[cd] Oleg V. Prezhdo*[cd] and WanZhen Liang*[ab]

Received 20th October 2021
Accepted 24th November 2021

DOI: 10.1039/d1ta09027e

rsc.li/materials-a

The mixed tin (Sn) and lead (Pb) perovskite compositions have shown great potential in perovskite photovoltaic devices due to the significantly enhanced material stability and prolonged carrier lifetime, compared to the pure Sn halide perovskites. In spite of the increasing interest, the behaviors of photo-generated charges and of the intrinsic point defects, such as the metal cation vacancies (V_{Sn} and V_{Pb}) and the interstitial halogen (i_I), have not been well understood in this class of materials. We report first-principles density functional theory (DFT) calculations combined with *ab initio* non-adiabatic molecular dynamics (NAMD) simulations on the static and dynamic structures of MA_2SnPbI_6 with and without these intrinsic defects. We discuss the nature of the defect states and unveil the influence of the intrinsic point defects on the structure, optoelectronic properties, and charge carrier dynamics of MA_2SnPbI_6. The i_I defect significantly shortens the carrier lifetime by creating mid-gap states that provide new recombination pathways. In comparison, the vacancy defects have much weaker influence on the carrier lifetime. Both V_{Sn} and V_{Pb} produce the defect states just below the valence band maxima (VBMs), and do not alter the band gap. They affect the carrier lifetime through changing the energy dispersions of VBMs and the conduction band minima (CBMs). We suggest that excess cations should be used in the synthesis of perovskites to avoid the appearance of interstitial halogen defects.

1 Introduction

Perovskite solar cells (PSCs) have been intensively studied in the past decade because of their high power-conversion-efficiency (PCE), low cost and easy synthesis.[1–7] The first PSC was designed by Miyasaka *et al.* with a PCE of only 3.8%.[3] Subject to the rapid advances over the past ten years, the certified PCE increased quickly to 29.5%.[8] These developments have demonstrated the great potential of PSCs as the next-generation low-cost solar technology. Unfortunately, the most efficient PSCs all contain Pb. The Pb-induced pollution and poisoning are serious environmental concerns, which have hampered the commercialization of the technologies based on these materials. Developing alternative strategies to minimize the impact of toxic Pb on the environment under the premise of maintaining the photoelectric activity of perovskite materials has become an important topic in perovskite photovoltaics.[2,7,9–11]

To reduce or eliminate the content of Pb, scientists have suggested to develop PSCs containing less Pb and Pb-free PSCs.[12–16] One idea is to develop Pb-free PSCs by replacing Pb with other elements. The earliest suggestion was to replace Pb with Sn and Ge, group 14 elements with comparable ionic radii.[17,18] Later, transition metals such as Cu, Mn, Fe, Co, and Ni were identified as promising alternatives to Pb, owing to their rich chemistries and multiple oxidation states. However, these Pb-free compounds suffer from poor efficiency and stability.

Another idea is to replace two divalent Pb(II) ions with monovalent and trivalent ions. Experimentalists have successfully synthesised double perovskites by using heterovalent substitution with monovalent Cu, Ag, Au or even alkali-metals, and trivalent In, Sb, and Bi cations.[19–32] However, these kinds of Pb-free perovskite materials possess serious flaws in optoelectronic properties, which make them less likely candidates for PSCs. For example, the most easily synthesized Ag–Bi and Ag–Sb double perovskites[19,20,23,33] have an indirect band gap, which will lead to a large amount of solar energy dissipated into heat after the carrier excitation.[34]

---

[a] *State Key Laboratory of Physical Chemistry of Solid Surfaces, Collaborative Innovation Center of Chemistry for Energy Materials, Fujian Provincial Key Laboratory of Theoretical and Computational Chemistry, People's Republic of China. E-mail: liangwz@xmu.edu.cn*

[b] *Department of Chemistry, College of Chemistry and Chemical Engineering, Xiamen University, Xiamen, Fujian 361005, People's Republic of China*

[c] *Department of Chemistry, University of Southern California, Los Angeles, California 90089, USA. E-mail: prezhdo@usc.edu*

[d] *Department of Physics and Astronomy, University of Southern California, Los Angeles, California 90089, USA*

† Electronic supplementary information (ESI) available. See DOI: 10.1039/d1ta09027e

The PCE of Ag–Bi double perovskite-based PSCs is much lower than that of Pb-based, and even Sn-based PSCs. It is about 1.25% in its maximum.[33] In addition, because AgI is highly sensitive to light, this kind of material cannot be filled with iodide cations, resulting in a wide band gap. The bulk phase of the In(I)–Bi(III) based perovskite has been predicted theoretically.[35] It has a direct band gap and a carrier effective mass similar to that of the traditional Pb-bearing materials. However, the stability of monovalent In^+ is lower than that of Ag^+ and Tl^+, and it has been reported experimentally that $Cs_2In(\text{I})In(\text{III})X_6$ perovskites are stable only at high temperature, while low temperature can cause a rotation between In(I) octahedra and In(III) octahedra, which leads to further degradation.[36]

An increasing number of studies have shown that it is difficult to eliminate Pb from high-performance PSCs. The more stable and better performing photoelectric materials are those still containing Pb, but in reduced amounts.[18,37–46] In such compounds, Pb is partially replaced by other elements, including Sn, Ge, Sr, or other alkaline-earth-metals. At present, the practical scheme is to adopt a mixed Sn–Pb composition, and to decrease the Pb content as much as possible, in order to reduce the environmental toxicity of Pb while maintaining the working stability of the device. For instance, Ramirez *et al.* adopted a 1 : 1.5 stoichiometric Sn : Pb ratio and reported a relatively high PCE of 10.5%.[47] Kapil *et al.* produced a spike structure of the Pb–Sn mixed perovskite and reached a 17.6% PCE.[48] Lanzetta *et al.* explained the surface-oxidation mechanism of Pb–Sn based perovskites.[49] Long *et al.*[50] discovered that the presence of Sn enhances the carrier lifetime of the traditional Pb-bearing perovskites.

When Sn(II) is exposed to air, it oxidizes spontaneously to form Sn(IV). Such a process leads to formation of various intrinsic defects,[42,51,52] which have a severe impact on the optoelectronic properties of the material.[53–63] The most common intrinsic defects generated in Pb–Sn perovskites include the Pb and Sn vacancies (V_{Pb} and V_{Sn}), and the interstitial iodide (i_I), which can be formed by the following chemical processes.

$$MASn(\text{II})I_3 + MAPbI_3 - 2e^- - Pb^{2+} = MASn(\text{IV}){I_3}^{2+} + MA[V_{Pb}]{I_3}^{2-};$$

$$MASn(\text{II})I_3 + MASn(\text{II})I_3 - 2e^- - Sn^{2+} = MASn(\text{IV}){I_3}^{2+} + MA[V_{Sn}]{I_3}^{2-};$$

$$MASn(\text{II})I_3 + I^- - 2e^- = MASn(\text{IV}){I_3}^{2+} + {i_I}^-.$$

In this work, we study the structure, and the static and dynamic properties of the mixed Pb–Sn perovskite, and elucidate how the structure, and the optoelectronic and photoelectric properties are influenced by the intrinsic defects that are formed by the oxidation of Sn(II). We perform both first-principles density functional theory (DFT) calculations and non-adiabatic molecular dynamics (NAMD) simulations to obtain the fundamental insights, guiding the construction of high performance PSCs. We generate a microscopic understanding of the characteristics of the materials with and without the intrinsic defects, and study the nature of the defect states, which usually play a decisive role in determining carrier recombination and diffusion lengths in solar cells, and explain why the photophysical properties of mixed Sn–Pb perovskites are enhanced considerably compared to those of Sn-based crystals.

2 Computational details

The first-principles DFT simulations were performed with the Vienna *Ab Initio* Simulation Package (VASP)[64–66] to study the geometric and electronic structures of the pristine and defective MA_2SnPbI_6 perovskite series. Unless otherwise specified, the generalized gradient approximation exchange-correlation functional of Perdew–Burke–Ernzerhof (PBE)[66] was adopted in the calculations. Since PBE tends to underestimate bandgaps, we employed the HSE06 functional[67,68] for benchmark calculations. HSE06 includes a fraction of screened Hartree–Fock exchange, $\alpha = 0.25$, improving the discontinuity in the Kohn–Sham potential derivative for integer numbers of electrons.

The spin–orbit coupling (SOC) effect is taken into account in the electronic structure calculations.

The electronic constituents are 4d 5s 5p for Sn, 5d 6s 6p for Pb, 5p 6s for I, 2s 2p for C and N, and 1s for H. For all the bulk-like systems, we adopted the Γ-point only for the HSE06 + SOC calculations, $4 \times 4 \times 4$ Γ-centered k-point grid generated by the Monkhorst–Pack scheme for detailed properties obtained with PBE + SOC, and $12 \times 12 \times 12$ linear scheme for the band-structure calculation with PBE + SOC. The projector augmented wave pseudopotentials with the cutoff energy of 500 eV were employed.

Considering the interaction between the hydrogen atoms and high-electronegativity groups, the PBE with the DFT-D3 dispersion correction of Grimme with zero-damping[69–71] was applied to optimize the geometric structures. During the optimization of the geometries, all structures were allowed to relax to ensure that each atom was in mechanical equilibrium without any residual force larger than 10^{-4} eV Å^{-1}.

Once the geometry optimization was completed, the repeated velocity rescaling was performed to equilibrate the structures at 300 K for 5 ps. Then, 8 ps adiabatic molecular dynamics trajectories were obtained within the microcanonical ensemble with the molecular dynamics time step set to 1 fs. To perform the NAMD simulations, we computed the non-adiabatic couplings d_{ij} using the time-domain numerical method[72] *via* the overlap between orbitals i and j at sequential time steps $d_{ij} = -i\hbar\langle|\phi_i|\nabla_R|\phi_j\dot{R}\rangle = -i\hbar\left\langle \phi_i\left|\frac{\partial}{\partial t}\right|\phi_j\right\rangle$ $= -i\hbar\frac{\langle\phi_i(t)|\phi_j(t+\Delta t)\rangle - \langle\phi_i(t+\Delta t)|\phi_j(t)}{2\Delta t}$.

The non-adiabatic coupling is proportional to the overlap of the wavefunctions between the initial (i) and final (j) states, $-i\hbar\langle\phi_i|\nabla_R|\phi_j\rangle$, and the nuclear velocity, dR/dt. The final 6000 configurations of the microcanonical molecular dynamics trajectories were selected as initial geometries for the following NAMD simulations of the nonradiative charge relaxation and electron–hole recombination with the Python extension for *Ab Initio* Dynamics code.[73,74] Since the structures had direct bandgaps located at the Γ-point, the NA couplings were computed for the Γ-point only.

3 Results and discussion

3.1 Geometric structures

At first, we optimize all the possible structures of pristine MA_2SnPbI_6 to determine which kind of topological arrangement of the metal cations gives the highest stability. For this reason, we build a few cubic perovskite-phase MA_2SnPbI_6 structures with different arrangements of Pb and Sn atoms, as shown in Fig. 1. Then, we optimize them and calculate their free energies. The results in Table 1 prove that the structure in Fig. 1(c) with the face-to-face arrangement of Pb and Sn atoms possesses the best thermal stability. This minimum unit cell is able to generate all internal point defects. Thus, this configuration is adopted in the later study at an affordable computational cost.

The influence of V_{Pb}, V_{Sn}, and i_I on the structure of MA_2SnPbI_6 is then explored. All the defective structures are relaxed with the lattice parameters fixed at the defect-free values to simulate point defects in a bulk crystal. To describe the influence of the defects on the system's geometry, we show the topological structure parameters of the defect-adjacent atoms in the flawed structures in Fig. 2 and Table 2, which demonstrate that when V_{Pb} or V_{Sn} appears, the average Sn–I bond lengths are longer than those without any defect. Thus, the atoms around the vacancies tend to move backwards the defect sites, so that the $[SnI_6]^{4-}$ octahedra are strongly distorted to accommodate these inert defects. However, it has weaker effect towards the structure of $[PbI_6]^{4-}$ octahedra. In addition, the vacancy defects flatten the metal-halide framework, as manifested in the increase of the average ∠M–X–M angles. For the i_I structure, the atoms around i_I are pulled away from the point defect by the adjacent framework, as reflected by the shorter bond lengths, smaller bond angles and distortion of M–X octahedral coordination.

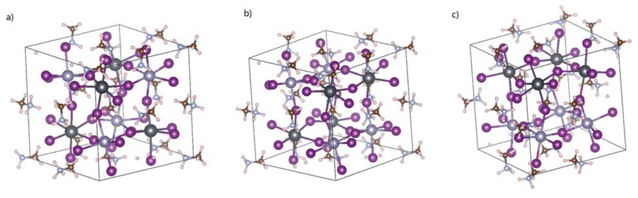

Fig. 1 Optimized structure of mixed Pb–Sn perovskite MA_2SnPbI_6.

Table 1 Geometric parameters and free energies for the MA_2SnPbI_6 structures without defects

Structures	(a)	(b)	(c)
a/Å	12.25	11.74	11.16
bÅ	12.23	12.25	12.20
c/Å	12.28	12.28	12.21
Free energy/eV	−417.302	−417.303	−417.360

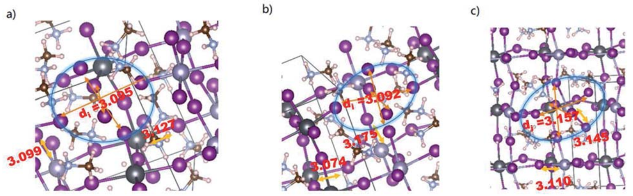

Fig. 2 Optimized defect-bearing structures of the MA_2SnPbI_6 perovskites: (a) V_{Pb}, (b) V_{Sn} and (c) i_I.

The formalism of DFE allows calculation of defect and impurity equilibrium structures and concentrations, and the relative stability of the different charge states of a given defect in the crystals.[75] We also calculated the relative DFEs of those point defects (see Table 2). The DFEs of charged defects are affected by the Fermi energy and the valence band level. The DFEs are expressed as[76] $\text{DFE} = E_{\text{defected}} - (E_{\text{perfect}} + \sum \varepsilon_{i,\text{dopants}}) + q(E_f + \text{VBM} + \Delta V_{\text{corr}}) + V_{\text{corr}}$, in which, E_f represents the Fermi energy, and ΔV_{corr} means the VBM potential correction with the bulk flawless phase reference. q denotes the charge state of a defect: for a neutral defect, $q = 0$, and if the defect structure has a positive charge, $q = 1$. V_{corr} is set for the electrostatic interaction correction between charged point defects in the periodically repeated supercells. In this work, the Makov–Payne approach[77] with the monopole approximation, $V_{\text{corr}} = \frac{\alpha q^2}{\varepsilon L}$, is adopted to calculate this term, in which the constant α represents the Madelung factor,[78–80] and ε is the dielectric constant obtained from the density functional perturbation theory.[81,82] The calculated DFEs demonstrate that i_I is generated most easily, followed by V_{Pb} and V_{Sn}. When a Sn(II) cation gets oxidized to Sn(IV), vacancy formation in the adjacent Pb(II) atoms is more likely than that in the Sn(II) atoms.

Considering that the intrinsic defects in actual system are often scattered in the lattice, we build a structure expressed as $MASn_{0.03125}Pb_{0.96875}I_3$, which possesses a large unit cell constructed by setting the minimum unit cell of MA_2SnPbI_6 shown in Fig. 1(c) in the center and surrounding it by the high-stability $MAPbI_3$ (see Fig. S1†). Then we investigated the influence of three kinds of point defects on the topological structure and calculate DFEs. The data shown in Table 2 and S1† tell that the

Table 2 The main geometric parameters and defect formation energy (DFE) of MA_2SnPbI_6 with and without defects. $\bar{d}i$ denotes the average distance for the vacancy-sharing atoms in the flawed crystal

Structures	Pristine	V_{Sn}	V_{Pb}	iI
d_{Sn-I}/Å	3.134	3.175	3.099	3.110
d_{Pb-I}/Å	3.185	3.074	3.127	3.145
∠Sn–I–Sn/°	154.2	161.1	156.4	147.2
∠Pb–I–Pb/°	153.5	165.6	167.8	153.2
min(∠M–X–M)°	148.6	146.6	148.2	108.2
$\bar{d}_i$/Å	—	3.092	3.095	3.157
DFE/(eV per cell)	—	+0.294	+0.128	+0.045

influence of internal defects on MA_2SnPbI_6 and $MASn_{0.03125}Pb_{0.96875}I_3$ is consistent. However, the defect-induced deformation on the $MASn_{0.03125}Pb_{0.96875}I_3$ lattice is slightly weaker than that on the MA_2SnPbI_6 lattice because of the tolerance of a large amount of stable $MAPbI_3$ in the former. The tolerance effect of the surrounding protective layer on the bond length of the defect-sharing atoms is less than 3%, indicating that the deformation on the defect-sharing structure is not affected by the lattice size. Therefore, to achieve a better balance between the computational cost and accuracy, we adopt the MA_2SnPbI_6 structure for later study.

3.2 Electronic and optoelectronic properties

Before NAMD calculations and carrier recombination analysis, we first make a static energy band analysis of the electronic structure. The band structure and projected density-of-states (pDOSs) of MA_2SnPbI_6 with and without the defects are plotted in Fig. 4 and S3–S5.†

The calculated band gap of MA_2SnPbI_6 is between those of $MAPbI_3$ (1.57 eV) and $MASnI_3$ (1.28 eV) by HSE06 + SOC, attributed to the hybridization of inert Pb-6s orbitals (with a minor 6p contribution) and active Sn-5s orbitals (with a minor 5p contribution) in the VBM. The CBM of MA_2SnPbI_6 is also composed of Pb-6p, Sn-5p and I-5p. i_I creates a characteristic deep defect state (DDS) lying in the band gap near the Fermi level, which is 0.43 eV above the VBM, and 0.26 eV below the CBM. This DDS is composed of the I-5p orbital of the interstitial I^-, and its energy dispersion $E(k)$ is nearly flat.

The characteristic defect states created by V_{Pb} and V_{Sn} are located below the VBMs, and they thus do not change the width of the band gap. However, the vacancies create several impurity states under the VBM and change the energy dispersions, indicating that they will play a role in the carrier migration and recombination. The pDOS in Fig. S3† shows that V_{Sn} weakens the contribution of Sn-5s to the VBM and CB edge states, while V_{Pb} had no such severe influence. The contribution of Pb-6s orbitals to the pDOS starts at lower energies compared to Sn-5s, and therefore, the influence of V_{Pb} on the VBM near the Fermi level is weaker than that of V_{Sn}. The charge distributions of the pristine and flawed MA_2SnPbI_6 are shown in Fig. S4.†

The relative mobility of the charge carriers can be characterized by the carrier effective masses.[83,84] The effective masses are calculated by fitting the energy dispersions of the VBM and the CBM to quadratic functions as $\frac{1}{m_{ii}^*} = \frac{1}{\hbar^2}\frac{\partial^2 E_n(\kappa_i)}{\partial {\kappa_i}^2} (i = x, y, z)$, where m_{xx}, m_{yy}, and m_{zz} correspond to the components in the x, y, and z directions, respectively. The results calculated for MA_2SnPbI_6 with and without defects are shown in Fig. 3(b).

When Sn atoms are present in the structure, the effective electron mass of the CBM ($\bar{m}c$) is very close to or even slightly lower than that of the pure Pb-based perovskite (approx. 5%[85]), indicating higher electron carrier mobility. Introduction of V_{Pb} and i_I can inhibit the electron mobility to a certain extent, and V_{Sn} has no obvious effect on it. In addition, these intrinsic defects have a significant impact on the hole mass in the VBM ($\bar{m}v$), especially i_I.

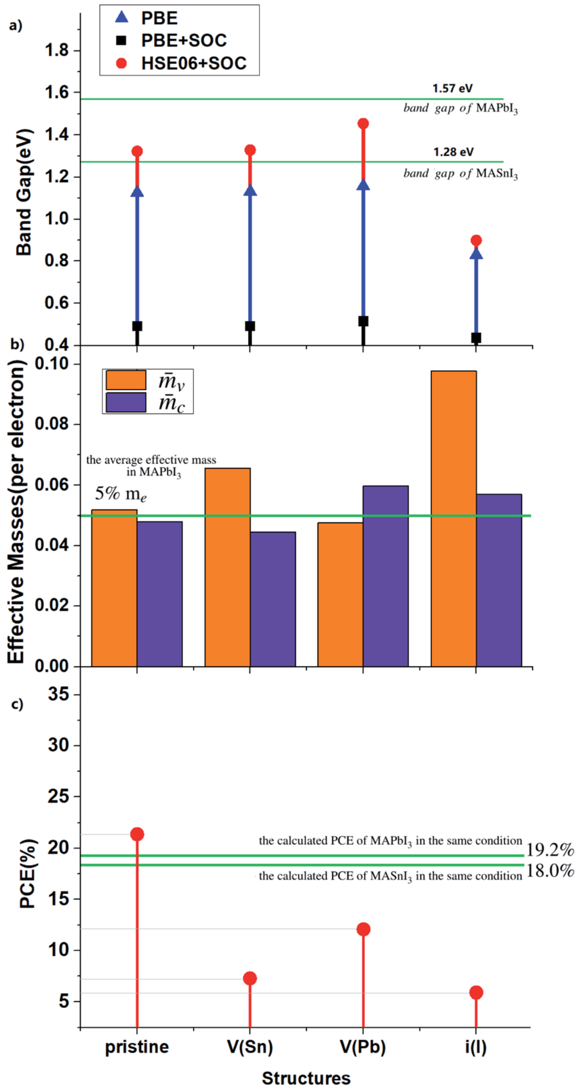

Fig. 3 (a) Band gaps calculated by PBE, PBE + SOC and HSE06 + SOC. (b) Effective masses and (c) PCEs calculated by PBE + SOC for the perfect and defective MA_2SnPbI_6. Comparison is made with the pure Pb-based and Sn-based perovskites.

V_{Sn} and V_{Pb} insert defect states below the VBM, and increase the energy dispersion of the VBM without changing the band gap magnitude. Since the VBMs arise mainly from the Sn-5s orbitals, V_{Sn} reduces the VBM dispersion more significantly. In other words, vacancy defects, such as V_{Sn} and V_{Pb}, make the VBM more localized.

The band gap is a key property of a light-to-energy conservation device, putting limits on its efficiency. Photons with a lower energy than the band gap cannot be absorbed efficiently, while electron–hole pairs generated above the band gap usually relax to the band edges, so that only part of the absorbed energy can be turned into work. In this sense, the absorption spectrum directly determines the PCE value. Hereafter, we adopt the spectral-limited maximum efficiency method as the PCE descriptor, going beyond the band gap, as suggested by Yu and Zunger[86,87] to calculate the number of photons absorbed by

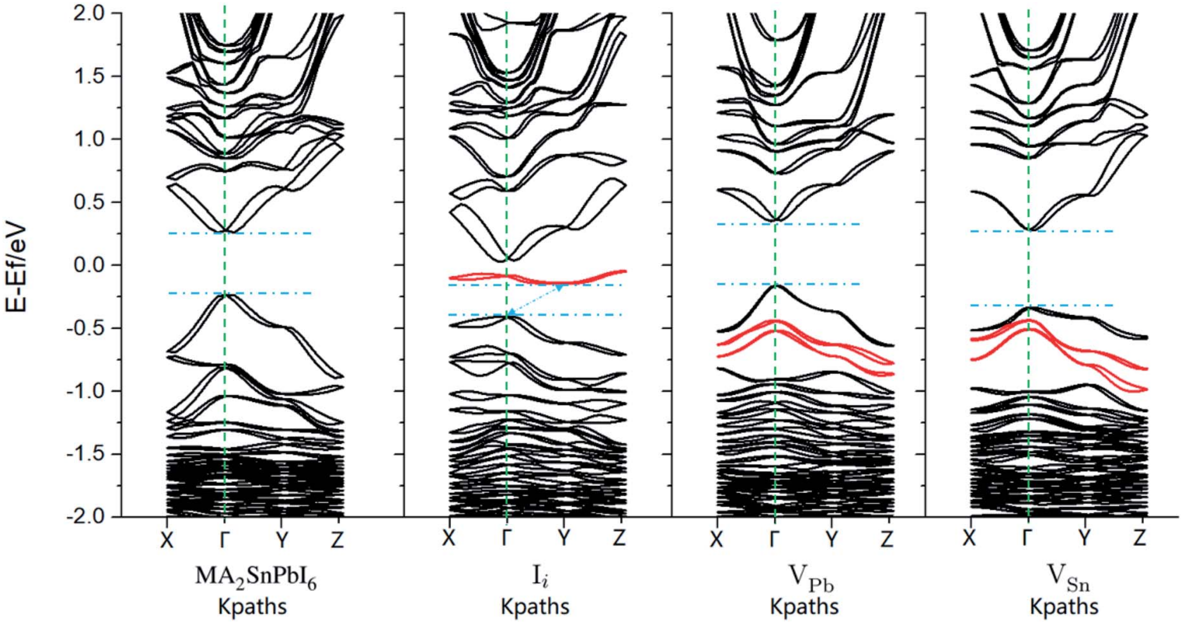

Fig. 4 Band structure of MA_2SnPbI_6 (a) without and (b–d) with intrinsic defects calculated by PBE + SOC. The red lines highlight the bands created by the intrinsic defects.

each structure. The efficiency, η, is obtained as $\eta = \frac{1}{n_{\mathrm{tot}}}\int_{E_{\mathrm{g}}^{\mathrm{dir}}}^{\infty} \mathrm{ph}_{\mathrm{abs}}(E)n_{\mathrm{ph}}(E)\mathrm{d}E$. Here, n_{tot} is the total number of photons emitted by the sun at AM1.5,[88] $\mathrm{ph}_{\mathrm{abs}}(E)$ is the photon absorptivity characteristic of the material, and $n_{\mathrm{ph}}(E)$ represents the number of sun photons at the energy, E, in the unit of eV. In this model, no absorption occurs below the direct bandgap, $E_{\mathrm{g}}^{\mathrm{dir}}$, since absorption through an indirect transition requires a change in the electron momentum assisted by phonons.

The calculated PCEs of the materials under investigation corresponding to the same optoelectronic device thickness (shown in Fig. S6†) are shown in Fig. 3(c) and S5 and S6.† The calculated results show that the band gap of pristine MA_2SnPbI_6 is closer to the Shockley–Queisser limit value of 1.37 eV (ref. 89) than the $MAPbI_3$ and $MASnI_3$ band gaps. Therefore, it exhibits higher PCE. All three point defects decrease the PCE. V_{Pb} has the weakest impact on the electronic structure and PCE. V_{Sn} decreases the PCE more than V_{Pb}. The DDS induced by i_I greatly changes the band structure and has the most serious impact on the PCE.

3.3 Electron–hole recombination and hot electron relaxation

In order to quantitatively describe the influence of the intrinsic defects on the carrier lifetimes, we have performed a series of NAMD simulations on the photexcited carrier relaxation and electron–hole recombination processes for the perfect and defective structures. Considering the computational effort, the NAMD simulations are based on the PBE functional without SOC since the band gaps calculated by PBE without SOC are much closer to those obtained by HSE06 + SOC than the band gaps obtained by PBE + SOC, and NAMD calculations based on HSE06 + SOC are too computationally demanding. The calculated non-adiabatic coupling (NAC) matrices are shown in Fig. S7.†

Fig. 5 shows the pure-dephasing functions calculated using the second order cumulant expansion as $D(t) = \exp\left(-\frac{1}{\hbar^2}\int_0^t \mathrm{d}t' \int_0^t \mathrm{d}t'' C(t'')\right)$. This optical response function characterizes the vibrationally induced pure-dephasing process for a pair of states entangled in a coherent superposition. It can be obtained directly or *via* the second-order cumulant expansion,[90] which allows notably better convergence. Pure-dephasing is associated with fluctuations of electronic energy levels due to coupling to phonons. The fluctuations are characterized by the energy gap autocorrelation function (ACF). The un-normalized ACF is defined as $C(t) = \langle \Delta E(t)\Delta E(0)\rangle$. It represents an ensemble average of the correlation of the energy gap fluctuation. A rapid decay of the ACF implies fast pure-dephasing. The ACFs characterize memory of the energy gap fluctuation.

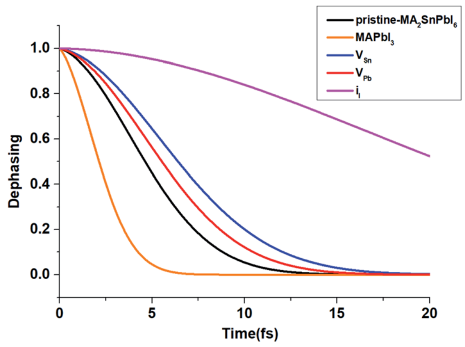

Fig. 5 Calculated pure-dephasing function of MA_2SnPbI_6 with and without defects. The result comparison is made with $MAPbI_3$.

Generally, shorter pure-dephasing time leads to slower dynamics, as exemplified by the quantum Zeno effect.[91] The pure-dephasing times depend most strongly on the magnitude of the phonon-induced fluctuation of the corresponding electronic energy gap.[92] Fig. S8(a)† shows the un-normalized ACF of the energy gap fluctuation, and the ACF initial values characterize the fluctuation magnitude. The fluctuation is the largest for the pristine system, resulting in the fastest decay of the pure-dephasing function. The i_I defect exhibits slower pure-dephasing, because the corresponding energy gap and its fluctuation are the smallest.

Fourier transform of the ACF produces the spectral density $I(\omega) = \left|\frac{1}{2\pi}\int_{-\infty}^{\infty} \mathrm{d}t\ \exp(-\mathrm{i}\omega t)C(t)\right|^2$. As shown in Fig. S8(b),† the calculated spectral densities characterize the phonon modes that couple to the electronic subsystem. Low-frequency modes play a predominant role, corresponding to twisting and stretching motion of the $[PbI_6]^{4-}$ and $[SnI_6]^{4-}$ octahedra, according to the previous research.[93,94]

To determine the time scales τ of the non-radiative electron–hole recombination, we obtain 30 ps of NAMD data, and fit the state populations to the short-time, linear approximation of exponential decay, *i.e.*, $P(t) = \exp(-t/\tau) \approx 1 - t/\tau$. Table 3 demonstrates that the carrier lifetime of the MA_2SnPbI_6 mixed perovskite is between those of $MAPbI_3$ and $MASnI_3$. Due to the higher VBM energy, pristine MA_2SnPbI_6 possesses a smaller band gap, and therefore, exhibits a shorter carrier lifetime than $MAPbI_3$. On the other hand, the incorporation of Pb into the Sn-based perovskite increases the carrier lifetime compared with that of the pure Sn-based perovskite. All the defective MA_2SnPbI_6 perovskites exhibit shorter carrier lifetimes than the pristine system. This can be traced to smaller initial values of the unnormalized ACF and longer pure-dephasing times. The carrier lifetimes of the perovskites with the cation vacancies are shorter because the VBM state is mixed with the defect states formed in the VB, Fig. 6(a). The V_{Sn} defect influences the electronic states near the VBM more strongly than the V_{Pb} defect, because it is energetically closer to the VBM, and notably hybridizes the VBM and deeper VB state, Fig. S3.† As a result, V_{Sn} changes the nonradiative charge recombination between the VBM and CBM more significantly than V_{Pb}. Changes in the spatial distributions of charges near the VBM and the CBM, Fig. S4,† are an important reason for variation of the carrier lifetime in different structures.[96]

The i_I-bearing system exhibits much faster nonradiative carrier recombination than the other systems studied in this work, Fig. 6. The DDS plays a decisive role here. The i_I creates DDS, Fig. 4(a), splitting the band gap into two smaller gaps, 0.43 eV + 0.26 eV by PBE + SOC. Nonradiative transitions across small energy gaps are fast, resulting in quick carrier quenching. 32% of active carriers recombine within the 30 ps NAMD simulation and 14% of them are captured by the interstitial DDS, Fig. 6(b).

Table 3 Calculated time scales of the carrier recombination for MA_2SnPbI_6 with and without defects. Comparison is made with $MAPbI_3$ and $MASnI_3$

Structure	SnPb	V_{Pb}	V_{Sn}	i_I	all-Pb	all-Sn[95]
τ/ns	54.88	20.11	5.72	0.441	159.6	8.37

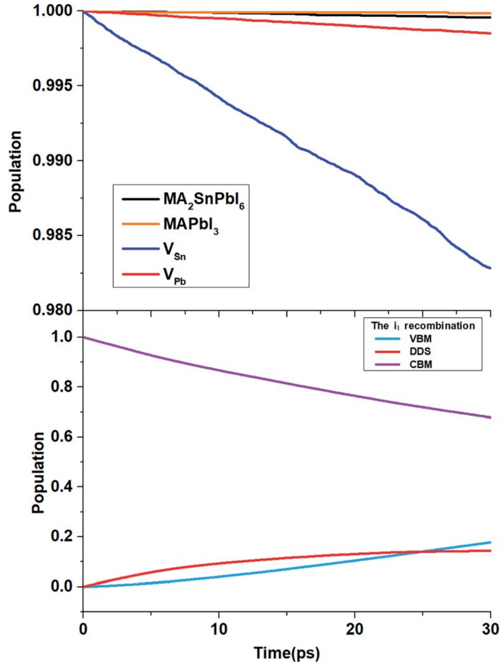

Fig. 6 Electron–hole recombination process from the CBM to the VBM for MA_2SnPbI_6 with and without defects.

To unveil the effect of these point defects on the carrier relaxation process, we simulate the hot electron relaxation dynamics from the low-lying CB edge states to the CBM, as shown in Fig. 7. Considering hot charge carriers at energies away from the band edges can provide advantages in solar energy applications, such as faster charge separation and transport, generation of additional carriers, and reduced

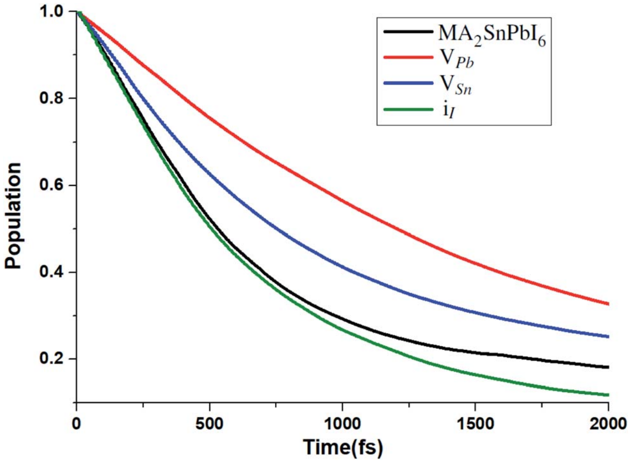

Fig. 7 Hot electron relaxation process from CBM + 1, CBM + 2 and CBM + 3 to the CBM for MA_2SnPbI_6 with and without defects.

trapping,[97] here we include all the relaxation effects from CBM + 1, CBM + 2 and CBM + 3 to the CBM.

The CB edges are mainly composed of Sn-5s 5p and Pb-6s6p orbitals (see Fig. S3†). Therefore, V_{Pb} and V_{Sn} significantly weaken the contribution of Pb and Sn to CB edges, leading to the increase of the relaxation time. The calculated carrier relaxation times τ for the V_{Pb}- and V_{Sn}-bearing structures are 2.02 and 1.29 ps, respectively. Because the i_I defect creates the mid-gap states and hardly affects the deep CB states, the carrier relaxation time of the i_I-bearing structure ($\tau = 0.97$ ps) is nearly the same as that of the defect-free structure ($\tau = 1.01$ ps).

4 Concluding remarks

We have performed first-principles DFT calculations combined with NAMD simulations on the static and dynamic characteristics of MA_2SnPbI_6 with and without intrinsic point defects, and compared its properties with those of its pure counterparts $MASnI_3$ and $MAPbI_3$. Meantime, in order to discuss the stability of defects in the realistic system as accurately as possible, we also calculated the geometric structures and defect formation energies of $MASn_{0.03125}Pb_{0.96875}I_3$ with a large supercell. This study unveils the nature of defect states and reveals how the intrinsic defects in the mixed Pb–Sn perovskite frameworks affect the electronic and geometric structures, the electron-vibrational coupling, the hot electron relaxation times, and the times of the nonradiative electron–hole recombination process at the ambient temperature. The following conclusions can be extracted from this study.

(1) The oxidation of Sn(II) results in the generation of many intrinsic defects such as V_{Sn}, V_{Pb} and i_I in the MA_2SnPbI_6 material. i_I can be most easily generated, followed by V_{Pb} and V_{Sn}. When one Sn(II) atom is oxidized, its adjacent Pb(II) atoms are prone to forming a defective vacancy, prior to Sn(II) atoms, and once a defect appears nearby, the $[SnI_6]^{4-}$ octahedra are always distorted more severely than $[PbI_6]^{4-}$ octahedra. It has been noted that Sn–Pb mixed perovskite materials possess an important feature: when Sn(II) is oxidized to Sn(IV), an adjacent Pb-vacancy forms, which will partially tolerate the negative impact of Sn(IV) on the photoelectric properties of Sn–Pb mixed perovskite materials.

(2) V_{Pb}, V_{Sn} and i_I affect the crystal structure differently. V_{Pb} and V_{Sn} cause elongation and distortion of the MX octahedra around the defects. This is reflected in a displacement of the octagon geometric centers. The M–X bond lengths of the center ion increase to offset somewhat the distortion of the octahedral structure. i_I makes the two adjacent MX octahedra repel each other, manifested in the reduction of the M–X bond lengths. Additionally, the vacancy defects flatten the M–X framework, while i_I distorts it severely.

(3) The band gap width and the carrier lifetime of MA_2SnPbI_6 lie between those of $MAPbI_3$ and $MASnI_3$ because the orbital hybridization of Sn and Pb affects the energy level of its VBMs, which are composed of the Sn-5*s*5*p* and Pb-6s6p orbitals. MA_2SnPbI_6 exhibits higher PCE than $MAPbI_3$ and $MASnI_3$ because its band gap width is much closer to the Shockley–Queisser limit. The tolerance of Pb-vacancy defects by the mixed Pb–Sn perovskite is also reflected in the electronic structure. The CBMs of MA_2SnPbI_6 are predominantly composed of the Sn-5p orbitals so that removing a Pb atom has a nearly negligible impact on its CB-related properties. Therefore, we can conclude that the existence of Pb atoms can inhibit the degradation arising from Sn oxidation in MA_2SnPbI_6. This is of great significance for maintaining the photoelectric activity of Sn-bearing perovskites.

(4) The point defects shorten the carrier lifetime of the material in the following order, V_{Pb}, V_{Sn} and i_I, with i_I giving the fastest carrier losses. The i_I defect creates deep defect states in the middle region of the band gap, which introduce new carrier recombination pathways, leading to a significant decrease of the carrier lifetime and the PCE. 32% of the carriers are lost within 30 ps due to the nonradiative electron–hole recombination in the presence of i_I and 14% of them are captured by the deep defect states created by the i_I defect. In order to avoid formation of the i_I defects, we suggest to decrease the anion content, or increase the cation content, to prevent the generation of i_I during nucleation of the crystal. Both V_{Sn} and V_{Pb} do not create defect levels in the band gap. However, they alter the energy dispersions of both the VBM and the CBM, changing the carriers' mobility and lifetime. The V_{Sn} defect weakens hybridization of the Pb and Sn orbitals, such that the Sn-5s and 5p orbitals contribute to the VBM very weakly around the defect. V_{Pb} has less impact on the material than V_{Sn}, because Pb atoms contribute less to the VBM edge states.

(5) Contrary to their influences on the electron–hole recombination process, the three kinds of point defects exhibit an impact on the hot carrier relaxation process with the order of i_I, V_{Sn} and V_{Pb}. i_I hardly affects the relaxation and both V_{Pb} and V_{Sn} slow down the relaxation, attributed to the defect-induced different changes on the energy dispersions of CB edge states.

This study establishes the microscopic mechanisms underlying the simultaneous improvement of the perovskite stability and the charge carrier lifetime by the hybrid cation strategy. It reveals the nature of the defect states and the influence of the intrinsic defects on the structures and optoelectronic properties, as well as the charge carriers' mobility and lifetimes. The general and fundamental principles established by analysis of the simulation results are useful for design of advanced materials for solar energy and optoelectronic applications.

Conflicts of interest

There are no conflicts to declare.

Acknowledgements

Financial support from the National Natural Science Foundation of China (Grant Nos 21833006 and 22173074) and the USA National Science Foundation (Grant No. CHE-1900510) is acknowledged.

Notes and references

1 A. Jena, A. Kulkarni and T. Miyasaka, Halide Perovskite Photovoltaics: Background, Status, and Future Prospects, *Chem. Rev.*, 2019, **119**, 3036–3103.

2 S. D. Stranks and H. J. Snaith, Metal-Halide Perovskites for Photovoltaic and Light-Emitting Devices, *Nat. Nanotechnol.*, 2015, **10**, 391–402.

3 A. Kojima, K. Teshima, Y. Shirai and T. Miyasaka, Light Sensitizers for Photovoltaic Cells, *J. Am. Chem. Soc.*, 2009, **131**, 6050–6051.

4 J. H. Noh, S. H. Im, J. H. Heo, T. N. Mandal and S. I. Seok, Chemical Management for Colorful, Efficient, and Stable Inorganic-Organic Hybrid Nanostructured Solar Cells, *Nano Lett.*, 2013, **13**, 1764–1769.

5 W. Yu, F. Li, L. Yu, M. R. Niazi, Y. Zou, D. Corzo, A. Basu, C. Ma, S. Dey, M. L. Tietze, T. Wu and A. Amassian, Single Crystal Hybrid Perovskite Field-Effect Transistors, *Nat. Commun.*, 2018, **9**, 1–10.

6 J. Huang, Y. Yuan, Y. Shao and Y. Yan, Understanding the Physical Properties of Hybrid Perovskites for Photovoltaic Applications, *Nat. Rev. Mater.*, 2017, **2**, 17042–17119.

7 M. Grätzel, The Light and Shade of Perovskite Solar Cells, *Nat. Mater.*, 2014, **13**, 838–842.

8 National Renewable Energy Laboratory, *Best Research-Cell Efficiencies*, http://www.nrel.gov/pv/cell-efficiency.html, 2021.

9 M. Lira-Cantu, Stability Lies at Interfaces, *Nat. Energy*, 2017, **2**, 17115.

10 S. Battersby, The Solar Cell of the Future, *Proc. Natl. Acad. Sci.*, 2019, **116**, 7–10.

11 S. Chen, Y. Deng, H. Gu, S. Xu, S. Wang, Z. Yu, V. Blum and J. Huang, Trapping lead in perovskite solar modules with abundant and low-cost cation-exchange resins, *Nat. Energy*, 2020, **5**, 1003–1011.

12 P. P. Boix, S. Agarwala, T. M. Koh, N. Mathews and S. G. Mhaisalkar, Perovskite Solar Cells: Beyond Methylammonium Lead Iodide, *J. Phys. Chem. Lett.*, 2015, **6**, 898–907.

13 C. Liu, W. Li, J. Fan and Y. Mai, A brief review on the lead element substitution in perovskite solar cells, *J. Energy Chem.*, 2018, **27**, 1054–1066.

14 V. K. Ravi, B. Mondal, V. V. Nawale and A. Nag, Don't Let the Lead Out: New Material Chemistry Approaches for Sustainable Lead Halide Perovskite Solar Cells, *ACS Omega*, 2020, **5**, 29631–29641.

15 F. Giustino and H. J. Snaith, Toward Lead-Free Perovskite Solar Cells, *ACS Energy Lett.*, 2016, **9**, 1233–1240.

16 Y. Fang, S. Zhai, L. Chu and J. Zhong, Advances in Halide Perovskite Memristor from Lead-Based to Lead-Free Materials, *ACS Appl. Mater. Interfaces*, 2021, **13**, 17141–17157.

17 F. Hao, C. C. Stoumpos, Z. Liu, R. Chang and M. G. Kanatzidis, Controllable Perovskite Crystallization at a Gas-Solid Interface for Hole Conductor-Free Solar Cells with Steady Power Conversion Efficiency over 10%, *Nat. Photonics*, 2014, **8**, 489–494.

18 N. K. Noel, S. D. Stranks, A. Abate, C. Wehrenfennig, S. Guarnera, A. A. Haghighirad, A. Sadhanala, G. E. Eperon, S. K. Pathak, M. B. Johnston, *et al.*, Lead-free Organic-Inorganic Tin Halide Perovskites for Photovoltaic Applications, *Energy Environ. Sci.*, 2014, **7**, 3061–3068.

19 A. H. Slavney, T. Hu, A. M. Lindenberg and H. T. Karunadasa, A Bismuth-Halide Double Perovskite with Long Carrier Recombination Lifetime for Photovoltaic Applications, *J. Am. Chem. Soc.*, 2016, **138**, 2138–2141.

20 E. T. McClure, M. R. Ball, W. Windl and P. M. Woodward, Cs_2AgBiX_6 (X = Br, Cl): New Visible Light Absorbing, Lead-Free Halide Perovskite Semiconductors, *Chem. Mater.*, 2016, **28**, 1348–1354.

21 G. Volonakis, M. R. Filip, F. Giustino, A. A. Haghighirad, N. Sakai, B. Wenge and H. J. Snaith, Lead-Free Halide Double Perovskites via Heterovalent Substitution of Noble Metals, *J. Phys. Chem. Lett.*, 2016, **7**, 1254–1259.

22 F. Wei, Z. Deng, S. Sun, F. Xie, G. Kieslich, D. M. Evans, M. A. Carpenter, P. D. Bristowea and A. K. Cheethama, The Synthesis, Structure and Electronic Properties of a Lead-Free Hybrid Inorganic–Organic Double Perovskite $(MA)_2KBiCl_6$ (MA = methylammonium), *Mater. Horiz.*, 2016, **3**, 328–332.

23 M. R. Filip, S. Hillman, A. A. Haghighirad, H. J. Snaith and F. Giustino, Band Gaps of the Lead-Free Halide Double Perovskites $Cs_2BiAgCl_6$ and $Cs_2BiAgBr_6$ from Theory and Experiment, *J. Phys. Chem. Lett.*, 2016, **7**, 2579–2585.

24 Z. Deng, F. Wei, S. Sun, G. Kieslich, A. K. Cheetham and P. D. Bristowe, Exploring the Properties of Lead-Free Hybrid Double Perovskites Using a Combined Computational-Experimental Approach, *J. Mater. Chem. A*, 2016, **4**, 12025–12029.

25 Y. J. Li, T. Wu, L. Sun, R. X. Yang, L. Jiang, P. F. Cheng, Q. Q. Hao, T. J. Wang, R. F. Lu and W. Q. Deng, Lead-free and Stable Antimony-Silver-Halide Double Perovskite $(CH_3NH_3)_2AgSbI_6$, *RSC Adv.*, 2017, **7**, 35175–35180.

26 M. Pazoki, M. B. Johansson, H. Zhu, P. Broqvist, T. Edvinsson, G. Boschloo and E. M. Johansson, Bismuth Iodide Perovskite Materials for Solar Cell Applications: Electronic Structure, Optical Transitions, and Directional Charge Transport, *J. Phys. Chem. C*, 2016, **120**, 29039–29046.

27 G. Volonakis, A. A. Haghighirad, R. L. Milot, W. H. Sio, M. R. Filip, B. Wenger, M. B. Johnston, L. M. Herz, H. J. Snaith and F. Giustino, $Cs_2InAgCl_6$: A New Lead-Free Halide Double Perovskite with Direct Band Gap, *J. Phys. Chem. Lett.*, 2017, **8**, 772–778.

28 B. Yang, J. Chen, S. Yang, F. Hong, L. Sun, P. Han, T. Pullerits, W. Deng and K. Han, Lead-Free Silver-Bismuth Halide Double Perovskite Nanocrystals, *Angew. Chem., Int. Ed.*, 2018, **57**, 5359–5363.

29 X. G. Zhao, J. H. Yang, Y. Fu, D. Yang, Q. Xu, L. Yu, S. H. Wei and L. Zhang, Design of Lead-Free Inorganic Halide Perovskites for Solar Cells via Cation-Transmutation, *J. Am. Chem. Soc.*, 2017, **139**, 2630–2638.

30 A. H. Slavney, L. Leppert, A. Saldivar Valdes, D. Bartesaghi, T. J. Savenije, J. B. Neaton and H. I. Karunadasa, Small-Band-Gap Halide Double Perovskites, *Angew. Chem., Int. Ed.*, 2018, **57**, 12765–12770.

31 X. Zhao, D. Yang, Y. Sun, T. Li, L. Zhang, L. Yu and A. Zunger, Cu–In Halide Perovskite Solar Absorbers, *J. Am. Chem. Soc.*, 2017, **139**, 6718–6725.

32 Q. Liu and W. Z. Liang, Structure and property tunability in monolayer halide lead-free double hybrid perovskites: effects of Rashba and biaxial strain, *J. Mater. Chem. A*, 2019, **7**, 11487–11496.

33 M. Pantaler, K. Cho, V. Queloz, B. Garcia, C. Fettkenhauer, I. Anusca, M. Nazeeruddin, D. Lupascu and G. Grancini, Hysteresis-Free Lead-Free Double-Perovskite Solar Cells by Interface Engineering, *ACS Energy Lett.*, 2018, **3**, 1781–1786.

34 M. R. Filip, S. Hillman, A. A. Haghighirad, H. J. Snaith and F. Giustino, Band Gaps of the Lead-Free Halide Double Perovskites $Cs_2BiAgCl_6$ and $Cs_2BiAgBr_6$ from Theory and Experiment, *J. Phys. Chem. Lett.*, 2016, **7**, 2579–2585.

35 G. Volonakis, A. A. Haghighirad, H. J. Snaith and F. Giustino, Route to Stable Lead-Free Double Perovskites with the Electronic Structure of $CH_3NH_3PbI_3$: A Case for Mixed-Cation $Cs/CH_3NH_3/CH(NH_2)_{22}InBiBr_6$, *J. Phys. Chem. Lett.*, 2017, **8**, 3917–3924.

36 K. McCall, D. Friedrich, D. Chica, W. Cai, C. Stoumpos, G. Alexander, S. Deemyad, B. Wessels and M. Kanatzidis, Perovskites with a Twist: Strong In^{1+} Off-Centering in the Mixed-Valent $CsInX_3$ (X = Cl, Br), *Chem. Mater.*, 2019, **31**, 9554–9566.

37 W. Zhu, G. Xin, Y. Wang, X. Min, T. Yao, W. Xu, M. Fang, S. Shi, J. Shi and J. Lian, Tunable optical properties and stability of lead free all inorganic perovskites $Cs_2SnI_xCl_{6-x}$, *J. Mater. Chem. A*, 2018, **6**, 2577–2584.

38 M. G. Ju, J. Dai, L. Ma and X. C. Zeng, Lead-Free Mixed Tin and Germanium Perovskites for Photovoltaic Application, *J. Am. Chem. Soc.*, 2017, **139**, 8038–8043.

39 C. Stoumpos, L. Frazer, D. Clark, Y. Kim, S. Rhim, A. Freeman, J. Ketterson, J. Jang and M. G. Kanatzidis, Hybrid Germanium Iodide Perovskite Semiconductors: Active Lone Pairs, Structural Distortions, Direct and Indirect Energy Gaps, and Strong Nonlinear Optical Properties, *J. Am. Chem. Soc.*, 2015, **137**, 6804–6819.

40 I. Kopacic, B. Friesenbichler, S. Hoefler, B. Kunert, H. Plank, T. Rath and G. Trimmel, Enhanced Performance of Germanium Halide Perovskite Solar Cells through Compositional Engineering, *ACS Appl. Energy Mater.*, 2018, **1**, 343–347.

41 D. Umadevi and G. Watson, Quasiparticle GW Calculations on Lead-Free Hybrid Germanium Iodide Perovskite $CH_3NH_3GeI_3$ for Photovoltaic Applications, *ACS Omega*, 2019, **4**, 5661–5669.

42 T. B. Song, T. Yokoyama, C. C. Stoumpos, J. Logsdon, D. H. Cao, M. R. Wasielewski, S. Aramaki and M. G. Kanatzidis, Importance of Reducing Vapor Atmosphere in the Fabrication of Tin-Based Perovskite Solar Cells, *J. Am. Chem. Soc.*, 2017, **139**, 836–842.

43 A. Stroppa, D. Di Sante, P. Barone, M. Bokdam, G. Kresse, C. Franchini, M. H. Whangbo and S. Picozzi, Tunable Ferroelectric Polarization and its Interplay with Spin-Orbit Coupling in Tin Iodide Perovskites, *Nat. Commun.*, 2014, **5**, 5900.

44 D. B. Mitzi, C. A. Feild and W. T. Harrison, Conducting Tin Halides with a Layered Organic-Based Perovskite Structure, *Nature*, 1994, **369**, 467–469.

45 A. Goyal, S. McKechnie, D. Pashov, W. Tumas, M. van Schilfgaarde and V. Stevanovic, Origin of Pronounced Nonlinear Band Gap Behavior in Lead–Tin Hybrid Perovskite Alloys, *Chem. Mater.*, 2018, **30**, 3920–3928.

46 T. Nakamura, T. Handa, R. Murdey, Y. Kanemitsu and A. Wakamiya, Materials Chemistry Approach for Efficient Lead-Free Tin Halide Perovskite Solar Cells, *ACS Appl. Electron. Mater.*, 2020, **2**, 3794–3804.

47 D. Ramirez, K. Schutt, Z. Wang, A. J. Pearson, E. Ruggeri, H. J. Snaith, S. D. Stranks and F. Jaramillo, Layered Mixed Tin–Lead Hybrid Perovskite Solar Cells with High Stability, *ACS Energy Lett.*, 2018, **3**, 2246–2251.

48 G. Kapil, T. S. Ripolles, K. Hamada, Y. Ogomi, T. Bessho, T. Kinoshita, J. Chantana, K. Yoshino, Q. Shen, T. Toyoda, T. Minemoto, T. N. Murakami, H. Segawa and S. Hayase, Highly Efficient 17.6% Tin–Lead Mixed Perovskite Solar Cells Realized through Spike Structure, *Nano Lett.*, 2018, **18**, 3600–3607.

49 L. Lanzetta, N. Aristidou and S. A. Haque, Stability of Lead and Tin Halide Perovskites: The Link between Defects and Degradation, *J. Phys. Chem. Lett.*, 2020, **11**, 574–585.

50 R. Shi and R. Long, Hole Localization Inhibits Charge Recombination in Tin–Lead Mixed Perovskites: Time–Domain ab Initio Analysis, *J. Phys. Chem. Lett.*, 2019, **10**, 6604–6612.

51 N. L. Lanzetta, N. Aristidou and S. A. Haque, Stability of Lead and Tin Halide Perovskites: The Link between Defects and Degradation, *J. Phys. Chem. Lett.*, 2020, **11**, 574–585.

52 B. Li, B. Chang, L. Pan, Z. Li, L. Fu, Z. He and L. Yin, Tin-Based Defects and Passivation Strategies in Tin-Related Perovskite Solar Cells, *ACS Energy Lett.*, 2020, **5**, 3752–3772.

53 D. Son, S. Kim, J. Seo, S. Lee, H. Shin, D. Lee and N. Park, Universal Approach toward Hysteresis-Free Perovskite Solar Cell via Defect Engineering, *J. Am. Chem. Soc.*, 2018, **140**, 1358–1364.

54 S. Wang, Y. Jiang, E. Juarez-Perez, L. Ono and Y. Qi, Accelerated degradation of methylammonium lead iodide perovskites induced by exposure to iodine vapour, *Nat. Energy*, 2017, **2**, 16195.

55 W. Yin, T. Shi and Y. Yan, Unusual defect physics in $CH_3NH_3PbI_3$ perovskite solar cell absorber, *Appl. Phys. Lett.*, 2014, **104**, 063903.

56 Q. Liu and W. Z. Liang, How the Structures and Properties of Pristine and Anion Vacancy Defective Organic–Inorganic Hybrid Double Perovskites $MA_2AgIn(Br_xI_{1-x})_6$ Vary with Br Content x, *J. Phys. Chem. Lett.*, 2020, **11**, 10315–10322.

57 W. Li, Y. She, A. S. Vasenko and O. V. Prezhdo, Ab initio nonadiabatic molecular dynamics of charge carriers in metal halide perovskites, *Nanoscale*, 2021, **13**, 10239–10265.

58 W. Chu, W. A. Saidi, J. Zhao and O. V. Prezhdo, Soft Lattice and Defect Covalency Rationalize Tolerance of β-$CsPbI_3$ Perovskite Solar Cells to Native Defects, *Angew. Chem., Int. Ed.*, 2020, **59**, 6435–6441.

59 R. Li, R. Wang, Y. Yuan, J. Ding, Y. Cheng, Z. Zhang and W. Huang, Defect Origin of Emission in $CsCu_2I_3$ and Pressure-Induced Anomalous Enhancement, *J. Phys. Chem. Lett.*, 2020, **12**, 317–323.

60 X. Zhang, Q. Ma, R. Li, C. Lin, D. Huang and Y. Cheng, The mechanism of alkali doping in $CsPbBr_3$: A first-principles perspective, *J. Appl. Phys.*, 2021, **129**, 165110.

61 Z. Gan, Y. Cheng, W. Chen, K. P. Loh, B. Jia and X. Wen, Photophysics of 2D Organic–Inorganic Hybrid Lead Halide Perovskites: Progress, Debates, and Challenges, *Adv. Sci.*, 2021, **8**, 2001843.

62 Y. Li, C. Zhang, X. Zhang, D. Huang, Q. Shen, Y. Cheng and W. Huang, Intrinsic point defects in inorganic perovskite $CsPbI_3$ from first-principles prediction, *Appl. Phys. Lett.*, 2017, **111**, 162106.

63 Z. Nan, L. Chen, Q. Liu, S. Wang, Z. Chen, S. Kang, J. Ji, Y. Tan, Y. Hui, J. Yan, Z. Xie, W. Liang, B. Mao and Z. Tian, Revealing phase evolution mechanism for stabilizing formamidinium-based lead halide perovskites by a key intermediate phase, *Chem*, 2021, **7**, 2513.

64 G. Kresse, Ab-Initio Molecular-Dynamics for Liquid-Metals, *J. Non-Cryst. Solids*, 1995, **193**, 10239–10265.

65 P. E. Blöchl, Projector Augmented-Wave Method, *Phys. Rev. B: Condens. Matter Mater. Phys.*, 1994, **50**, 17953–17979.

66 J. P. Perdew, K. Burke and M. Ernzerhof, Generalized Gradient Approximation Made Simple, *Phys. Rev. Lett.*, 1996, **77**, 3865–3868.

67 J. Heyd and G. E. Scuseria, Assessment and validation of a screened Coulomb hybrid density functional, *J. Chem. Phys.*, 2004, **120**, 7274.

68 J. Heyd, G. E. Scuseria and M. Ernzerhof, Hybrid functionals based on a screened Coulomb potential, *J. Chem. Phys.*, 2003, **118**, 8207.

69 S. Grimme, Semiempirical GGA-type density functional constructed with a long-range dispersion correction, *J. Comput. Chem.*, 2006, **27**, 1787–1799.

70 S. Grimme, J. Antony, S. Ehrlich and H. Krieg, A consistent and accurate ab initio parametrization of density functional dispersion correction (DFT-D) for the 94 elements H-Pu, *J. Chem. Phys.*, 2010, **132**, 154104.

71 J. Moellmann and S. Grimme, DFT-D3 Study of Some Molecular Crystals, *J. Phys. Chem. C*, 2014, **118**, 7615–7621.

72 T. Verteśi, Á. Vibók, G. J. Halász, A. Yahalom, R. Englman and M. Baer, The Electronic Non-Adiabatic Coupling Matrix: A Numerical Study of the Curl Condition and the Quantization Condition Employing the Mathieu Equation, *J. Phys. Chem. A*, 2003, **107**, 7189–7196.

73 A. V. Akimov and O. V. Prezhdo, The PYXAID Program for Non-Adiabatic Molecular Dynamics in Condensed Matter Systems, *J. Chem. Theory Comput.*, 2013, **9**, 4959–4972.

74 A. V. Akimov and O. V. Prezhdo, Advanced Capabilities of the PYXAID Program: Integration Schemes, Decoherence Effects, Multiexcitonic States, and Field-Matter Interaction, *J. Chem. Theory Comput.*, 2014, **10**, 789–804.

75 C. Freysoldt, B. Grabowski, T. Hickel and J. Neugebauer, First-principles Calculations for Point Defects in Solids, *Rev. Mod. Phys.*, 2015, **86**, 253–305.

76 D. Meggiolaro and F. de Angelis, First-Principles Modeling of Defects in Lead Halide Perovskites: Best Practices and Open Issues, *ACS Energy Lett.*, 2018, **3**, 2206–2222.

77 G. Makov and M. C. Payne, Periodic Boundary Conditions in Ab-Initio Calculations, *Phys. Rev. B: Condens. Matter Mater. Phys.*, 1995, **51**, 4014–4022.

78 B. Nijboer and F. De Wette, On the calculation of lattice sums, *Phys. D*, 1957, **23**, 309–321.

79 L. Glasser, Solid-State Energetics and Electrostatics: Madelung Constants and Madelung Energies, *Inorg. Chem.*, 2012, **51**, 2420–2424.

80 R. P. Grosso, J. T. Fermann and W. J. Vining, An In-Depth Look at the Madelung Constant for Cubic Crystal Systems, *J. Chem. Educ.*, 2001, **78**, 1198.

81 K. Refson, P. Tulip and S. Clark, Variational density-functional perturbation theory for dielectrics and lattice dynamics, *Phys. Rev. B: Condens. Matter Mater. Phys.*, 2006, **73**, 155114.

82 S. Wu, D. Vanderbilt and D. Hamann, Systematic treatment of displacements, strains, and electric fields in density-functional perturbation theory, *Phys. Rev. B: Condens. Matter Mater. Phys.*, 2005, **72**, 035105.

83 M. G. Ju, G. X. Sun, Y. Zhao and W. Z. Liang, A Computational View of the Change in the Geometric and Electronic Properties of Perovskites Caused by the Partial Substitution of Pb by Sn, *Phys. Chem. Chem. Phys.*, 2015, **17**, 17679–17687.

84 J. Feng and B. Xiao, Effective Masses and Electronic and Optical Properties of Nontoxic $MASnX_3$ (X = Cl, Br, and I) Perovskite Structures as Solar Cell Absorber: A Theoretical Study Using HSE06, *J. Phys. Chem. C*, 2014, **118**, 19655–19660.

85 S. Chatterjee and A. Pal, Influence of metal substitution on hybrid halide perovskites: towards lead-free perovskite solar cells, *J. Mater. Chem. A*, 2018, **6**, 3793–3823.

86 L. Yu and A. Zunger, Identification of Potential Photovoltaic Absorbers Based on First-Principles Spectroscopic Screening of Materials, *Phys. Rev. Lett.*, 2012, **108**, 068701.

87 I. E. Castelli, K. S. Thygesen and K. W. Jacobsen, Calculated optical absorption of different perovskite phases, *J. Mater. Chem. A*, 2015, **3**, 12343–12349.

88 *Reference Solar Spectral Irradiance: Air Mass 1.5*, http://rredc.nrel.gov/solar/spectra/am1.5/hmtl.

89 W. Shockley and H. J. Queisser, Detailed Balance Limit of Efficiency of p–n Junction Solar Cells, *J. Appl. Phys.*, 1961, **32**, 510–519.

90 S. Mukamel, *Principles of Nonlinear Optical Spectroscopy*, 1995.

91 S. V. Kilina, A. J. Neukirch, B. F. Habenicht, D. S. Kilin and O. V. Prezhdo, Quantum Zeno effect rationalizes the phonon bottleneck in semiconductor quantum dots, *Phys. Rev. Lett.*, 2013, **110**, 180404.

92 A. V. Akimov and O. V. Prezhdo, Persistent Electronic Coherence Despite Rapid Loss of Electron-Nuclear Correlation, *J. Phys. Chem. Lett.*, 2013, **4**, 3857–3864.

93 A. M. Leguy, A. R. Goni, J. M. Frost, J. Skelton, F. Brivio, X. Rodriguez-Martinez, O. J. Weber, A. Pallipurath, M. I. Alonso, M. Campoy-Quiles, M. T. Weller, J. Nelson, A. Walsh and P. R. Barnes, Dynamic disorder, phonon lifetimes, and the assignment of modes to the vibrational

spectra of methylammonium lead halide perovskites, *Phys. Chem. Chem. Phys.*, 2016, **18**, 27051–27066.

94 C. Quarti, G. Grancini, E. Mosconi, P. Bruno, J. M. Ball, M. M. Lee, H. J. Snaith, A. Petrozza and F. de Angelis, The Raman Spectrum of the $CH_3NH_3PbI_3$ Hybrid Perovskite: Interplay of Theory and Experiment, *J. Phys. Chem. Lett.*, 2014, **5**, 279–284.

95 A. Li, Q. Liu, W. B. Chu, W. Z. Liang and O. V. Prezhdo, Why Hybrid Tin-Based Perovskites Simultaneously Improve the Structural Stability and Charge Carriers-Lifetime: Ab Initio Quantum Dynamics, *ACS Appl. Mater. Interfaces*, 2021, **13**, 16567–16575.

96 S. Banerjee, J. Kang, X. Zhang and L. Wang, The effects of interstitial iodine in hybrid perovskite hot carrier cooling: A non-adiabatic molecular dynamics study, *J. Chem. Phys.*, 2020, **152**, 091102.

97 T. Wang, L. Jin, J. Hidalgo, W. Chu, J. Snaider, S. Deng, T. Zhu, B. Lai, O. V. Prezhdo, J. Correa-Baena and L. Huang, Protecting hot carriers by tuning hybrid perovskite structures with alkali cations, *Sci. Adv.*, 2020, **6**, 1336.